Probing the Intermediates of Catalyzed Dehydration Reactions of Primary Amide to Nitrile in Plasmonic Junctions

Jianghao Zhou^{†,‡}, Jing Guo[‡], Alexander Moiseevich Mebel[§], Govinda Ghimire[‡], Feng Liang^{*,†}, Shuai Chang^{*,†} and Jin He^{*,‡,ξ}

[†]The State Key Laboratory of Refractories and Metallurgy, School of Materials and Metallurgy, School of Chemistry and Chemical Engineering, Wuhan University of Science and Technology, Wuhan, 430081, China.

‡Department of Physics, Florida International University, Miami, Florida 33199, USA.

§Department of Chemistry and Biochemistry, Florida International University, Miami, Florida 33199, USA.

EBiomolecular Science Institute, Florida International University, Miami, Florida 33199, USA

Keywords: plasmon-driven reaction, single-molecule reaction, amide dehydration, intermediates, SERS, picocavity.

ABSTRACT

Visible light can effectively drive chemical reactions in plasmonic molecular junctions owing to the high reactivity of adatoms at the surface of plasmonic metal nanostructures and the localized surface plasmon resonance (LSPR) induced energetic charge carriers (electrons and holes) and heat. Here, we investigated the dehydration reaction of primary amides, which is important to generate valuable nitrile molecules, in the visible-light irradiated self-assembled gold nanoparticlearomatic primary amide-gold nanoelectrode junctions in aqueous solution at the ambient conditions. At present, the research on the dehydration reaction of the primary amide group is only at the macroscopic level, limiting the mechanistic study of reaction dynamics and intermediates. Using time-resolved surface enhanced Raman spectroscopy (SERS) with 10s of millisecond time resolution, we successfully followed the evolution of the SERS spectra along with various transient spectral changes during the rise of nitrile vibration peak. Combined with density functional theory and picocavity model, we revealed most pronounced transient spectral changes were from the gold surface adatoms coupled reaction intermediates. The adatoms produced picocavities with strong atomic size local field, which strongly enhanced the SERS signals of the intermediates down to sub single-molecule resolution. The active adatoms played critical roles in producing, interacting and stabilizing the intermediates. We have determined the complex reaction pathway involving multiple proton transfer steps and intermediates with signature carbon-nitrogen double and triple bonds.

INTRODUCTION

Noble metal nanoparticles (NPs) such as gold NPs (GNPs) formed plasmonic molecular junctions have emerged as exciting nanoscale chemical reactors. Supported small GNPs are chemically reactive and have been used as effective heterogeneous catalysts in several chemical reactions at mild conditions. By shining visible light on the GNPs, the light energy can be harvested on the GNP surface through the localized surface plasmon resonance (LSPR), which further decays through the nonradiative pathways into heat and high-energy hot electrons and holes² to catalyze chemical reactions on the GNP surface.^{3, 4} The concentrated light field in the junctions can also greatly amplify signals of surface enhanced Raman spectroscopy (SERS), which has been used to monitor the organic reactions *in situ* and in real time up to the single-molecule level.⁵ To study the mechanism of chemical reactions, it is important to probe the intermediates. However, due to the transient and dynamic nature of the intermediates, the mechanistic study of organic reaction by SERS in plasmonic junctions is still limited to a few simple reactions with few intermediates, including C-C bond cleavage,⁶ C-C bond cross-coupling,⁷ and 4-aminothiophenol (4-ATP) oxidation⁸ and 4-nitrothiophenol (4-NTP) reduction to p,p'-dimercaptoazobisbenzene (DMAB).⁹

The dehydration of primary amide (-CONH₂) to produce nitrile is a century-old method in organic chemistry. Due to the importance of nitrile and primary amide, continued efforts till today have been made to improve the reaction efficiency and condition. ^{10, 11} The primary amide is a $p-\pi$ conjugated structure in which the carbonyl group is the electron withdrawing group and the nitrogen atom can donate electron by resonance to the adjacent carbonyl group. ¹² Therefore, the NH bond is weakened while the CN bond is strengthened. To overcome the energy penalty of dehydration, catalysts are needed to speed up the reaction in a mild condition. In the classical methods, the reaction is catalyzed in organic solvent using dehydrating agents. The oxygen atom of the carbonyl group is first attacked by the nucleophile of the catalyst, which triggers deprotonation of the amine group and the following deoxygenation to generate the nitrile. Recently, it has been shown that the reaction can also be catalyzed by a metal. ^{10, 13} However, the catalytic reactions are always studied in ensemble, and the reaction intermediates cannot be observed.

In this study, the heterogeneous chemical transformation from aromatic primary amide to aromatic nitrile was catalyzed in self-assembled plasmonic molecular nanojunctions and probed in an

aqueous solution by time-resolved SERS (see Fig. 1) with 10s of millisecond time resolution. The signature Raman peak of the nitrile group was observed, confirming the dehydration transformation can indeed happen in the plasmonic junction even in the aqueous solution, which is attributed to the cooperative catalyzation by both the undercoordinated gold adatoms and hot electrons in the plasmonic junction. This reaction is also reversible and the produced nitrile was observed to be hydrated back to amide. Rich but complex transient SERS signals were also observed in the time-resolved spectra about 10% of the time. Aided by density functional theory (DFT) calculations and the recently developed picocavity model, we have thoroughly investigated the origin of the most frequently observed dynamic signals. Most of those pronounced dynamic signals with peaks different from the reactant and product molecules are linked to the 'picocavities' enhanced signatures of individual intermediates from the amide dehydration reaction. In the junction, the surface gold atoms undergo dynamic surface reconstruction and form adatoms. They generate so-called 'picocavities', which cause extremely high electric field enhancement on the atomic scale¹⁴ and enable single-molecule SERS detection.^{15, 16} The reactive gold adatoms form various metal-molecule complexes with reaction intermediates, helping to stabilize both the picocaivity and the intermediate with prolonged average lifetime of about 10 s. Based on the identified intermediates, we determined the reaction pathway of primary amide dehydration reaction in the plasmonic junction.

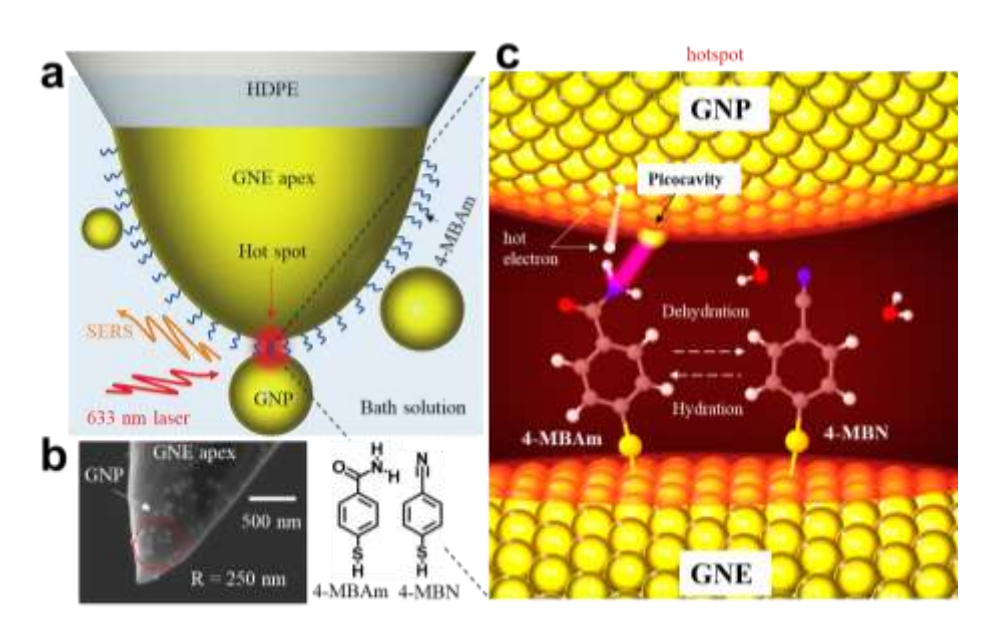


Figure 1 | SERS measurements of the dehydration reaction of aromatic primary amide 4-MBAm in a NPoNE junction. a. Schematic of the SERS measurement on the NPoNE plasmonic molecular junctions

formed by the adsorbed GNP on a high density polyethylene (HDPE) insulated GNE with 4-MBAm modified apex. **b**. Left, SEM image of a 4-MBAm modified GNE apex with adsorbed GNPs. Right, the molecular structures of reactant 4-MBAm and product 4-MBN. **c**. The diagram illustrates the catalyzed dehydration reaction of tethered 4-MBAm to produce nitrile (4-MBN) in the hotspot.

RESULTS AND DISCUSSIONS

The chemical reaction of primary amide in the plasmonic molecular junction

As shown in Fig. 1, SERS is conducted on the 4-mercaptobenzoamide (4-MBAm) modified gold nanoelectrode (GNE) apex. After adding 40 nm GNPs to the liquid cell, we monitored the evolution of SERS signals due to the adsorption of GNPs on the GNE apex. ¹⁷ Fig. 2a(i) shows the representative time-intensity SERS trajectory in heatmap format within 1 min after adding GNPs. Two pronounced peaks quickly appeared and enhanced near 1080 and 1592 cm⁻¹, suggesting the increased number of adsorbed GNPs and hotspots in the formed NP on NE structures (NPoNE). Following the two major peaks, two broad minor peaks near 1207 cm⁻¹ and 1412 cm⁻¹ gradually appear and become more obvious in some cases (see Fig. 2a(ii)). These peaks in the spectra are generally stable. A few minutes later, a new peak near 2237 cm⁻¹ often appears (see a(iii)). Along with the new peak, more dynamic spectral changes with transient new peaks have been observed in the spectral range of 1000-1600 cm⁻¹. The overall spectral intensity is generally stabilized in about 12 min. We then removed the free moving GNPs from the liquid cell and continued to monitor the spectral changes from the established NPoNE structures on the GNE apex. Based on the crude estimation (see section 3 of SI), there are less than 10 molecules in each hotspot and slightly over 1000 molecules in all the hotspots of the NPoNE structures.

The time-averaged SERS spectra after normalization for the three trajectories in Fig. 2a are shown in blue color in Fig. 2b. To understand the observed SERS peaks, we conducted DFT calculations of possible structures using Gaussian09 software (see Fig. S5(1)-(3)), including the Au5-4-MBAm complex interacting with a Au4 cluster or a water molecule. The calculated spectra of the latter (Fig. 2b (2)) matched well the one shown in a(i), indicating when the junction is just formed, the 4-MBAm is likely solvated with water molecules and only interacts weakly with the surface gold atoms of the GNP. The two major peaks are attributed to the stretching of benzene ring and are always observed in simple aromatic thiol molecules. According to the peak notations for two well-

studied aromatic thiol molecules 4-aminothiolphenol and 4-mercaptobenzoic acid, the peaks at 1080 cm^{-1} and 1592 cm^{-1} are referred to as 7a and 8a, respectively. We use the same notations here for convenience. The peak 7a is coupled with the v(C-S) vibration and is less affected by the changes of the amide group. Thus, we use this peak as the internal reference.

Between a(i) and a(ii), the main difference is in the growth of two minor peaks between 7a and 8a. The minor peak at 1414 cm⁻¹ is from $\nu(\text{CONH}_2)$ of 4-MBAm. The other minor peak near 1196 cm⁻¹ is missing in the calculated spectrum (2). One possible origin of this peak is from the deprotonated structure of 4-MBAm. The deprotonation of primary amide on the metal surface has been observed using SERS.¹⁸ In the deprotonated structure, which is named I1, a proton is removed from the nitrogen atom. As shown in (4) of Fig. 2b, the calculated spectrum from the molecular structure of the Au5/I1/Au5 complex features two minor peaks at 1222 cm⁻¹ and 1423 cm⁻¹, which are assigned to $\beta(\text{NH})$ and $\nu(\text{CONH}^-)$ of the I1 structure, respectively. They match well with the two broadened minor peaks in a(ii). We also did the calculation when the deprotonated nitrogen atom is only stabilized by a water molecule (see Fig. S5(7)), but the result did not match well with the one in a(ii).

The second possible origin of the two minor peaks is from the tautomer structure of 4-MBAm (named I2), whereby one proton is transferred from the nitrogen atom to oxygen atom. The tautomer structure has been previously observed in gold-4-MBAm-gold junction by single molecule conductance measurements.¹⁹ Indeed, a new minor peak of β(NH) near 1189 cm⁻¹ appears in the calculated spectrum based on the Au5/I2/H₂O complex (see Fig. S5 (4)-(5)). The peak near 1207 cm⁻¹ in spectra (3) is also difficult to be differentiated between I1 and I2 (see Fig. S5 (5)-(8)). Although there are small shifts in the peak positions, the two minor peaks of I1 and I2 cannot be separated in broadened minor peaks of the time averaged spectra a(i) and a(ii). Both spectra likely have contributions from 4-MBAm and its tautomer and deprotonated structures. Both I1 and I2 may appear shortly in the newly formed plasmonic junctions.

In a(iii), a unique peak near 2237 cm⁻¹ appears, which is most likely from the stretching vibration of nitrile group $(v(C \equiv N))$, $^{20, 21}$ indicating the appearance of 4-mercaptobenzonitrile (4-MBN) in the hotspots of NPoNE structures. In the calculated spectrum of Au5/4-MBN complex (Fig. 2b(7)),

the v(C = N) peak is even higher than peaks 7a and 8a. By simply adding the calculated spectra of 4-MBAm (Fig. 2b(2)) and 4-MBN (Fig.2b(7)) with 1:1 ratio (Fig.2b(6)), the new spectrum is closer to the averaged spectrum a(iii). Therefore, the spectrum a(iii) is contributed from both the reactant 4-MBAm and its product 4-MBN. In addition, the two middle peaks are more obvious, suggesting that I1 and I2 are also present.

Fig. 2c shows a representative SERS trajectory during the onset of the signature nitrile peak of 4-MBN near 2237 cm⁻¹. Fig. 2d shows the corresponding time trace of the peak area ratio $I_{A\nu(C=N)}/I_{A7a}$. The peak area (I_A) in the background corrected spectra (see S4 of SI) is proportional to the number of contributing molecules (N) through equation I_A =N σ , where σ is the relative cross section of the molecule. Based on the DFT calculation, the σ values of 7a are similar for both 4-MBAm and 4-MBN molecules thus I_{A7a} is proportional to the total number of molecules. Post $I_{A\nu(C=N)}$ is only from 4-MBN. Therefore, the peak area ratio $I_{A\nu(C=N)}/I_{A7a}$ is proportional to the number ratio of 4-MBN to total molecules in the hotspots. Large fluctuations are observed in the $I_{A\nu(C=N)}/I_{A7a}$ time trace in Fig.2d. Therefore, there are likely only a small number of 4-MBN molecules in the junctions and these newly produced 4-MBN molecules are not stable and may be transformed back into 4-MBAm by hydrolysis. However, the instability of gold adatoms may also contribute to some of the fluctuations. The 2237 cm⁻¹ peak appears most of the time (over 80%) of the measurements, suggesting the reaction is effective and the produced 4-MBNs present in the hotspots most of the time.

The chemical reaction from 4-MBAm to 4-MBN inside the plasmonic junction is likely catalyzed by plasmon and the gold nanostructures on the surfaces of GNP and GNE. To confirm the reaction is driven by plasmon, we measured the yield of 4-MBN under different laser power irradiations. As shown in Fig. 2e, the percentage of 4-MBN in the probable hotspots is plotted as a function of laser power. The results show that the number ratio of 4-MBN indeed increases with the laser power density. The plasmon-driven reaction maybe both induced by hot electron and plasmonic heating though a recent review suggests the latter is less likely due to the measured and calculated temperature increase is only in the order of 10s of kelvins in the hotspots.⁴ However, the temperature increase in the picocavities is more difficult to be probed.¹⁴ Because the picocavities

play important roles in the observed reactions here, we thus cannot exclude the contribution from the plasmonic heating. We also carried out control experiments by modifying the GNP surface with a layer of thiophenol molecules containing different end functional groups (see S6 of SI). The modified molecules not only suppress the effect of hot electrons generated at the gold surface but also interrupt the direct interaction and charge transfers between surface gold atoms of GNP and

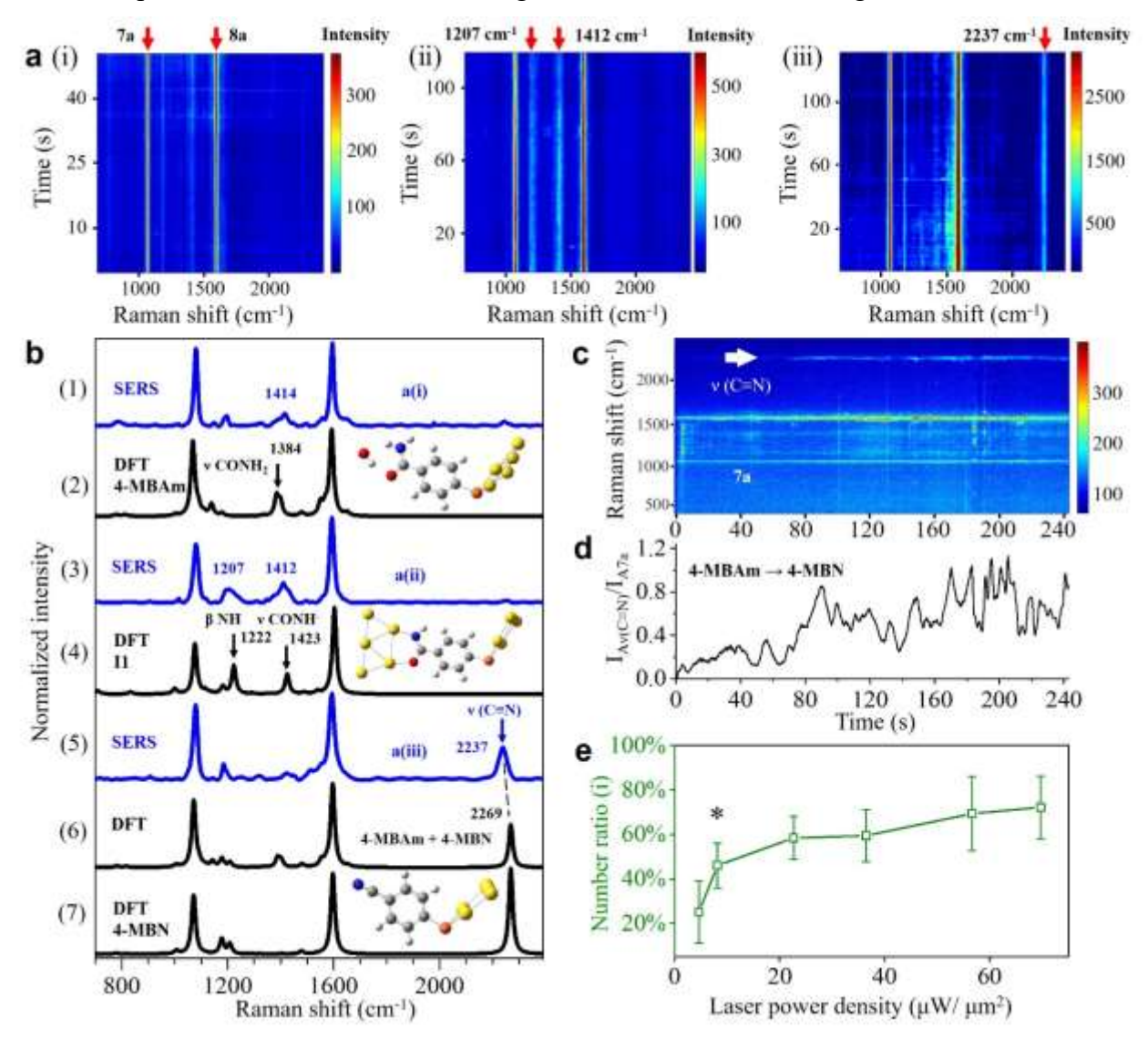


Figure 2 | The SERS results of catalyzed 4-MBAm to 4-MBN reaction in NPoNE structures. a. The stable SERS trajectory at early ((i) and (ii)) and later times (iii). b. The stacked spectra of 4-MBAm and 4-MBN from SERS measurements and DFT calculations. c. The SERS time trajectory of 4-MBN generation. d. The corresponding time trace of peak area ratio $I_{A\nu(C\equiv N)}/I_{A7a}$. e. The derived molecular number ratio of 4-MBN as a function of laser power density. The star indicates the number ratio is 46% at the typically

used laser power density (8.14 μ W/ μ m²). The error bar is the standard division of the results from 5 measurements.

the amide group of 4-MBAm. Among the amide, carboxyl and nitro functional groups, all three can suppress the appearance of the $v(C \equiv N)$ peak but only the nitro group can fully prevent it. This is because the hydrogen atom of carboxyl and amide groups can interact with the electron-rich oxygen atom of the primary amide and accept the electron transfer through the nucleophilic interaction. The nitro group instead has two electron-rich oxygen atoms, which can effectively block the electron transfer from the oxygen atom of the amide group, thus preventing the deprotonation process of amide group. These control experiments suggest the dehydration reaction of primary amides in the NPoNE structure is likely catalyzed by both the plasmon conditions and the gold nanostructures.

Probing the intermediate structures

We also observed multiple dynamic and transiently enhanced peaks suddenly rising above the stable spectra. These peaks usually last for a few to tens of seconds and their patterns are not fully random. One or a few peaks appear repeatedly, and some peaks often appear and disappear simultaneously. These highly dynamic and synchronized changes are most likely single-molecule level signals and associate with picocavities (see below). Here we will discuss three more frequently appeared signal patterns, named as s-1, s-3, and s-5. Another two less frequently appeared signals s-2 and s-4 are discussed in SI. To understand these signals, we first conducted the DFT calculations using QuantumATK software to search and optimize the possible atomic structures of the Au-molecule-Au complex for these dynamic signals. By using the periodic structure of the gold cluster, the interaction between the molecule and gold atoms can be better simulated. Then the Raman spectra of the final structures were calculated by using Gaussian09 software (for more details see method and section 7 of SI). The phenomena of a few suddenly appeared pronounced peaks cannot be generated by the single-molecule rotation motions.²⁴ Motivated by the recent picocavity studies in plasmonic junctions, 14-16 we also calculated and compared the vibration mode enhancement due to picocavities at different locations near the molecule (see S10 of SI). Based on the results of DFT calculation and the chemical reaction mechanism of dehydration reaction of primary amide, we found that the signals s-1 to s-5 were from the intermediate structures in the catalyzed reaction of the primary amide.

One example of s-1 is shown in the trajectory of Fig. 3a(i). Two new peaks are suddenly greatly enhanced at 109 s and lasted for about 66 s with significant intensity fluctuations. In Fig. 3b(i), two transient spectra taken from the trajectory before and after the onset of s-1 are compared. We also analyze the statistical distributions of the peak positions for both peaks (Fig. 3c(i)). Their mean values are 1277 cm⁻¹ and 1495 cm⁻¹. After conducting DFT calculations for more than 10 structures to match the two newly arise peaks, we determined that the s-1 signal was from the deprotonated structure I1. The proposed molecule-metal complex structure for s-1 is shown in Fig. 3d(i). Two gold adatoms interact simultaneously with both the nitrogen and oxygen atoms of I1, helping stabilize I1 and induce two major vibration modes $\beta(NH)$ and $\nu(CONH^{-})$. The peak positions of both vibration modes are sensitive to the gold-molecule interaction (see Fig. S15a of SI). Meanwhile, the gold adatoms near the oxygen and/or nitrogen atoms may produce picocavity effect, greatly enhancing the two modes of β (NH) near 1276 cm⁻¹ and ν (CONH⁻) near 1482 cm⁻¹. This is demonstrated by the blue lines in Fig. 3b(i), representing the calculated vibration modes after the picocavity enhancement effect based on the structure shown in Fig. 3d(i). As shown in Fig. S12, by positioning the picocavity at different locations, the enhancement, and wavenumbers for these two vibration modes can change dramatically. Similar to s-1, another picocavity stabilized I1 signal s-2 is discussed in S11 of SI.

Fig. 3a(ii) shows a representative SERS time trajectory containing s-3, which occurred from 58 s to 71 s with a pronounced new peak appearing at the left side of the 8a peak. The new peak is also obvious in the transient spectrum (red color) in Fig. 3b(ii). As shown in Fig. 3c(ii), its mean peak position is at 1525 cm⁻¹. This peak is also greatly enhanced in the anti-Stokes spectra (see Fig. S16), suggesting its picocavity origin. Based on DFT calculations (see Fig. S17), we also confirmed that this suddenly increased lone peak could only be simulated by introducing a highly localized electromagnetic field of picocavity. One final structure with a picocavity is shown in Fig. 3d(ii). The tautomer structure of 4-MBAm (I2) interacts with the protruded gold atom through the N atom. The undercoordinated gold atom at the top withdraws electron from the N atom, helping to stabilize I2. This gold atom also forms a picocavity to greatly enhance the v(C=N) mode, as shown by the calculated vibration modes in blue lines in Fig. 3b(ii). The enhancement is highly sensitive to the relative positions of the gold and nitrogen atoms (see Fig. S17). The peak position of the v(C=N) mode is greatly affected by the details of the Au-N interaction as shown in Fig. S18.

As we discussed in section 1, the signal of I2 is difficult to be isolated from others in the stable spectra. Here, the picocavity enhanced signal helps to confirm the existence of the tautomer structure I2.

Fig. 3a(iii) shows the SERS trajectory containing s-5 with a characteristic new peak near 2050 cm⁻¹ occurring from 10 s to 27 s. The corresponding transient spectra are shown in Fig. 3b(iii). Compared with the nitrile peak near 2232 cm⁻¹, this new peak is highly unstable and fluctuates significantly in its position and intensity. This is also demonstrated by comparing the broad distribution of this peak with the very narrow distribution of the nitrile peak (green color) in Fig. 3c(iii). Considering its spectral position and dynamic nature, we speculate that this new peak originates from an unstable and weakened nitrile group (or enhanced C=N double bond, named C ≅N here). The nitrile peak intensity and position are highly sensitive to the neighboring functional group and local solvation, electrostatic and chemical environment.²⁵ For example, with interaction to metal ions, the $C \equiv N$ triple bond is weakened and down shifted to about 2100 cm⁻¹. ^{16, 21, 26} We occasionally also observed a relatively stable small peak around 2130 cm⁻¹ next to the major nitrile peak. With stronger interactions, the C≡N triple bond can be further weakened and its vibration peak has been observed with further red-shifts to around 2000 cm⁻¹. From DFT calculations, this peak is likely from the C≌N bond of a transition structure named T5, which is the transition structure between intermediate I3 (see section S13 of SI) and the final product 4-MBN. In the simulated Au2/T5/Au5 complex structure (see Fig. 3d(iii)), the gold atom interacts with both the oxygen and nitrogen atoms, which stabilizes T5. The weakened C-O bond of T5 leads to the enhanced C=N double bond. As the orange color spectrum shown in Fig. 3b(iii), the calculated $\nu(C \cong N)$ peak of T5 matches very well with the signature peak of s-5. The peak intensity can also be enhanced by the gold atom interacting with the CN group, as shown by the blue line in Fig. 3b(iii).

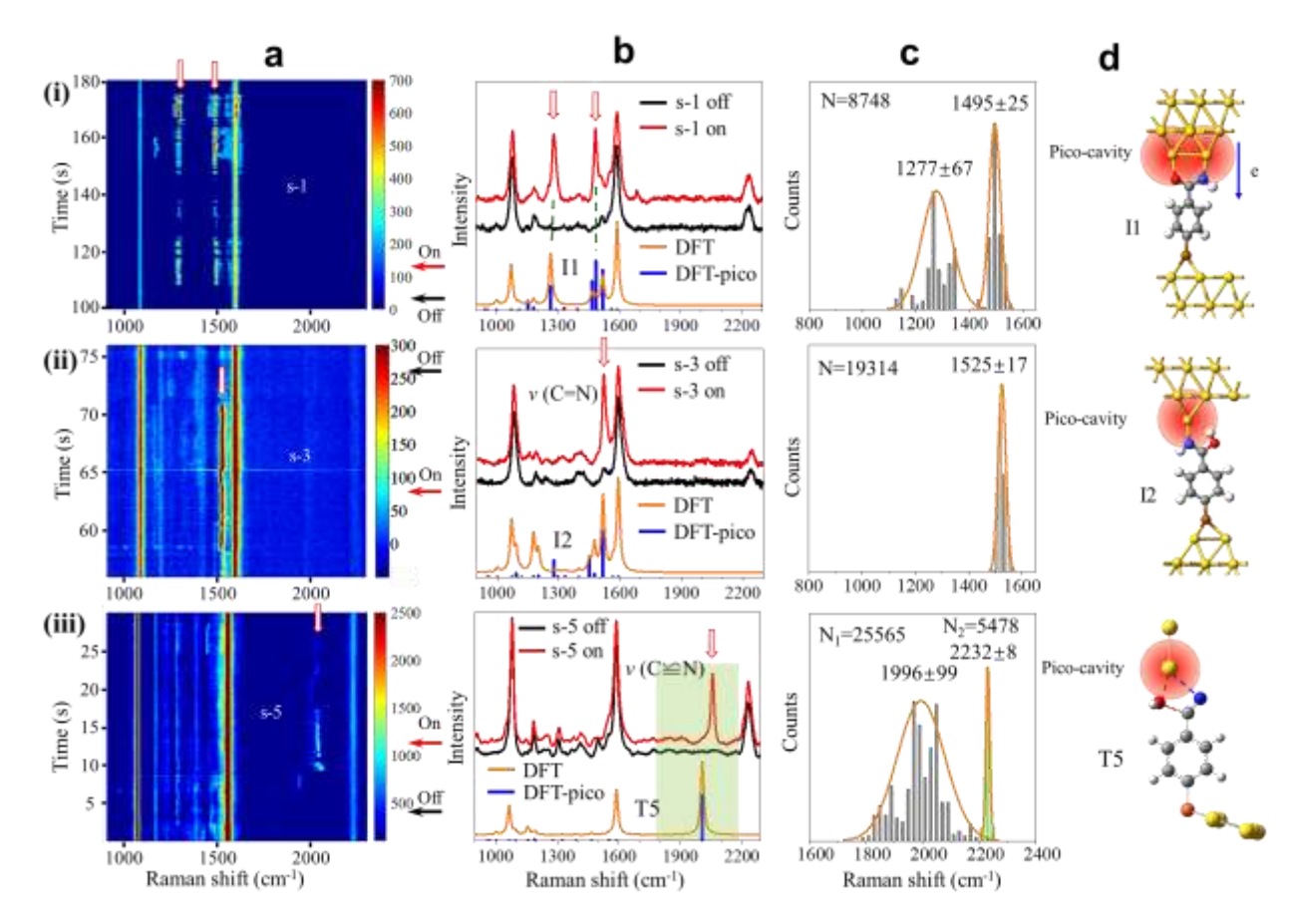


Figure 3 | The three frequently appeared dynamic signals (s-1 ((i)), s-3 ((ii)) and s-5 ((iii)). a. The representative SERS time trajectories. b. The two transient spectra when the signal is on (red) and off (black) at the time points indicated by the arrows in a. The spectra in orange color are the calculated spectra and the blue lines indicate the modes enhanced by the picocavities. c. The distributions of the spectral positions of the signature peaks. The N is the number of frames for each signal. The orange lines are the Gaussian fits. The error of the mean peak position is taken as the half width at half height of the fit. The green peak in (iii) is from the nitrile peak and used here for the comparison. d. The best-matched intermediate structures with picocavity positions for DFT calculations in b.

As shown in Fig. 4a, we also counted the number of occurrences (orange) and total occurrence times (green) for the four most frequently observed dynamic signals which is s-1, s-2, s-3 and s-5. It's worth noting that there are very few s-4 signals, so we have no statistics. We select only the individual signals with defined starting and ending times. The occurrence counts follow an order s-5 > s-3 > s-1 > s-2. The percentage of total occurrence time is calculated by dividing the total occurrence time of each type of signal by the total measurement time. All these signals can only be observed in less than 4% of the total measurement time. For the percentage of occurrence time,

that the statistical data here are only for the observable single-molecule signals. A lot of I1 and I2 signals may not be detected if they are not stabilized and amplified by the picocavities. In addition, the signature peak of T5 is outside the crowded spectral region and can be easily identified. Fig. 4b shows the lifetime distribution on the logarithmic scale for these signals. They all have a lifetime on the scale of 10 s. The gold adatom-intermediate interaction apparently plays an important role in extending the lifetime. The lifetime of s-2 is slightly longer than others, which could indicate that the picocavity generated by I1-Au interaction is more stable than others.

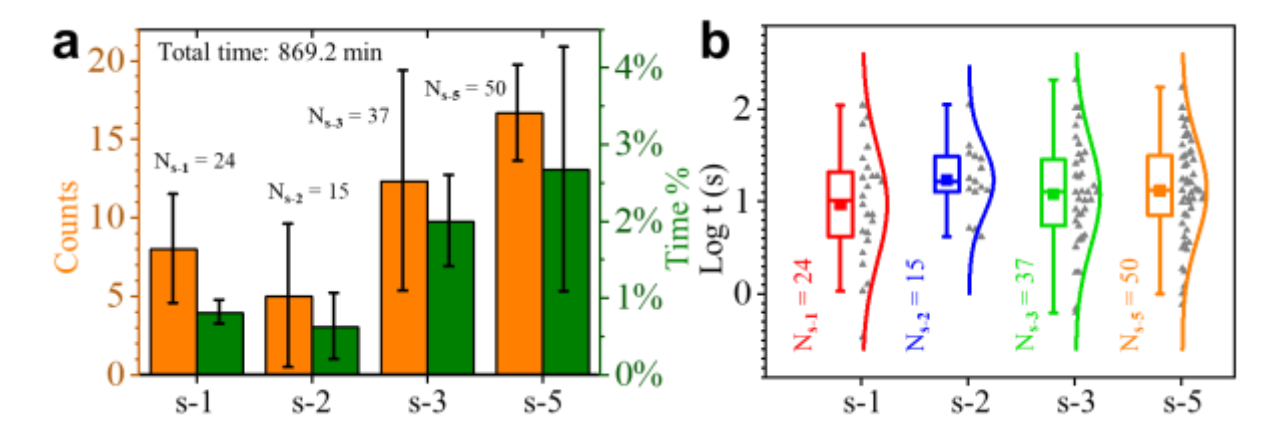


Figure 4 | The statistical results for four types of dynamic signals. a. The occurrence statistics for four dynamic signals. The orange columns represent the occurrence counts and the green columns represent the percentage of occurrence time over total recording time for each type of signal. The error bar is calculated based on three repeated experiments. b. The distributions of event lifetime in log scale are shown in the scatter plots (gray triangle dots). The solid lines are the Gaussian fits. The corresponding box charts are shown on the left side of the scatter plots. The solid square dots represent the mean values of the lifetime. The mean lifetimes of s-1, s-2, s-3 and s-5 are 9.3 s, 16.6 s, 11.9 s and 12.9 s, respectively. N is the total number of events from 3 repeated experiments.

Direct tracking the reaction dynamics

In the experiments, we observed not only the transiently appeared signals of individual intermediates, but also the dynamic transition between these intermediates. Several representative SERS trajectories are shown in Fig.5 and Fig. S21. The trajectory in Fig.5a shows the chemical transformation from I2 to T5. Three transient spectra during the dynamic conversion are shown in Fig.5b, which provides more details of the spectral changes. Near time point 220 s, s-3 signal with

its signature peak near 1539 cm⁻¹ appeared, suggesting the presence of I2. Near time point 242 s, signal s-3 suddenly disappeared, followed by the appearance of s-5 with its signature peak near 1821 cm⁻¹, suggesting the appearance of T5. The s-5 signal remained for around 56 s and then the spectra returned to the stable spectra of 4-MBAm and no new $v(C \equiv N)$ peak was observed. Therefore, the T5 likely returned to 4-MBAm instead of becoming the final product 4-MBN.

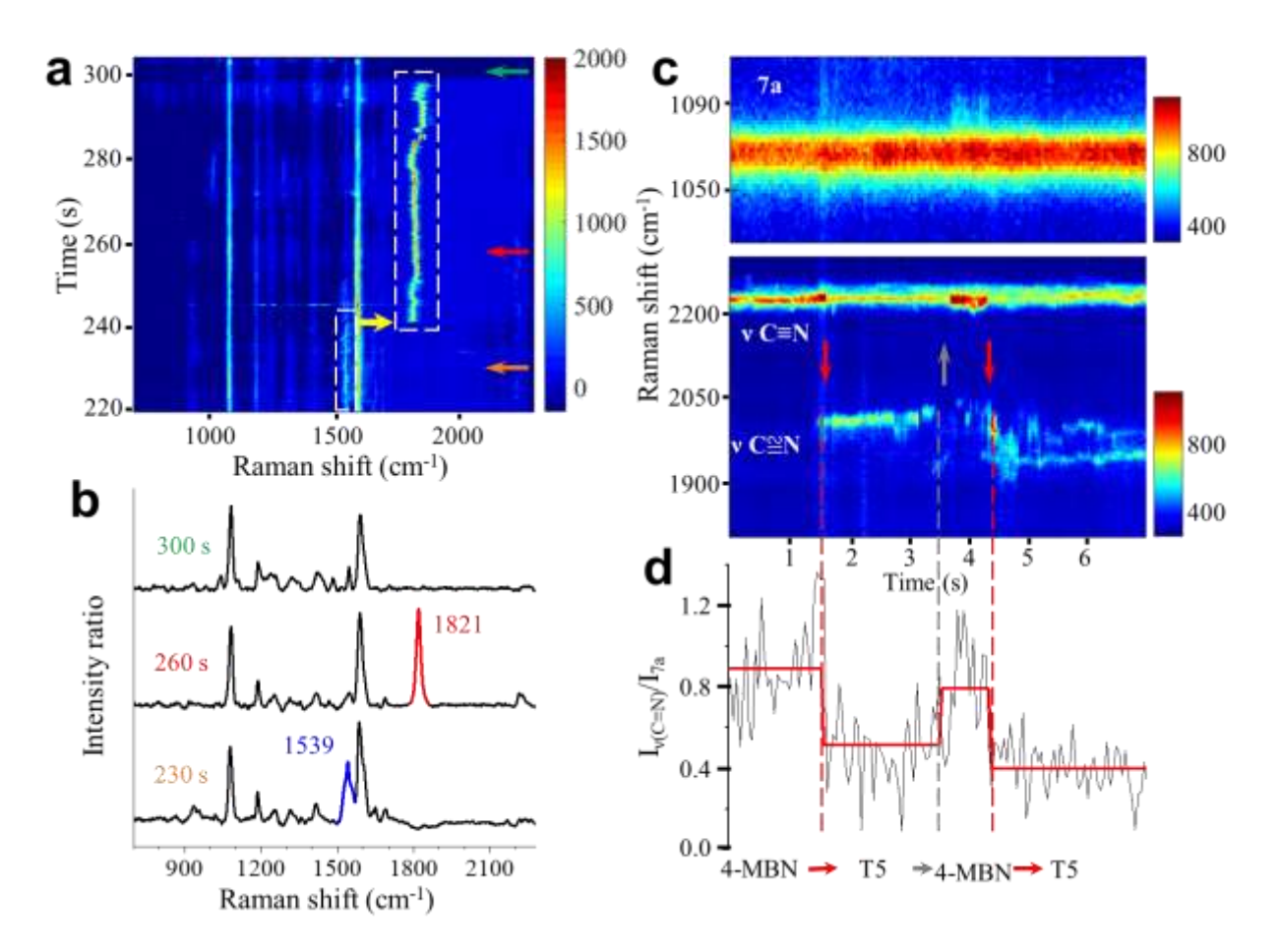


Figure 5 | Dynamic spectral changes of transformation between intermediate structures and 4-MBN product. a. Representative SERS trajectory of transformation from I2 to T5. b. Three transient spectra at the selected time points in a. c. Typical SERS trajectory in the heatmap of 7a (top panel), $v(C \cong N)$ and $v(C \cong N)$ modes (bottom panel) for the transitions between T5 and 4-MBN. d. The corresponding intensity ratio $(I_{v(C=N)}/I_{7a})$, black) time trace. The solid red line is the step function fitted curve.

Fig.5c shows another trajectory highlighting the changes in modes 7a, $\nu(C \cong N)$ and $\nu(C \equiv N)$ to show the reversible transitions between T5 and product 4-MBN. I_{7a} is almost unchanged, suggesting the overall light field in the hotspots is relatively stable. In contrast, significant spectral

changes are observed in the traces of the v(C = N) and v(C = N) modes. The v(C = N) mode is in the range of 1900~2050 cm⁻¹ and the v(C = N) mode is at around 2240 cm⁻¹. Interestingly, we found that the intensity changes of v(C = N) and v(C = N) modes are anti-correlated. For example, as indicated by the red arrows at 1.5 s and 4.3 s, the abrupt drop of $I_{v(C = N)}$ and the sharp increase of $I_{v(C = N)}$ happen simultaneously, reflecting the chemical transformation from 4-MBN to T5. Similarly, the spectral change at 3.5 s, as indicated by the gray arrow, suggests the conversion from T5 to 4-MBN. Fig.5d shows the corresponding time trace of the intensity ratio $I_{v(C = N)}/I_{7a}$ in which we selected the 7a mode as the internal reference because it is less affected by the reaction of the amide group. The stepwise changes of the intensity ratio reveal the reversible conversions between 4-MBN and T5 occurred in the junction. The anti-correlated changes strongly suggest the dynamic changes are from only one nitrile group in the hotspots.

Proposed reaction route of primary amide in a plasmonic junction.

To understand the experimental results, we have used DFT to calculate the Raman spectra and energies of many possible intermediates and transition states. Based on the experimental and calculation results, we propose the reaction pathway from 4-MBAm to 4-MBN in the plasmonic junctions, as illustrated in Fig.6a. The corresponding energy landscape is shown in Fig. 6b, which includes the energies for all intermediates along with the proposed reaction pathway and the corresponding transition states. The energies ($\Delta E + \Delta G$) are the sums of electronic and thermal free energies calculated at 298.15 K. In the reaction pathway, the interaction with the gold atom is required to complete the pathway. Water molecules may also be involved in the reaction pathway (see S22 of SI), which can slightly reduce the reaction energy barriers, especially in the first two steps for the amide-iminol tautomerism. The tautomer structure I2 has the lowest energy among the three intermediates, suggesting I2 is relatively stable. In this pathway, the rate-limiting step is the generation of I3 with a steep energy barrier of 2.4 eV. The energy barriers to reach all the intermediates are bigger than the room temperature thermal energy at 0.025 eV. Therefore, the hot electron generated in the plasmonic junction is necessary to catalyze these reactions. It should be mentioned that all these chemical transformations seem reversible in the plasmonic junction (see Fig. 5 and Fig. S21). For example, when a hydroxide ion attached to the gold adatom interacts strongly with the carbon atom of the 4-MBN nitrile group, the 4-MBN would first become T5 and then be hydrated back to become I2 or I1, coupled with the proton transfers.

As shown in the first two steps, the reaction is initiated by the amide-iminol tautomerism, induced by the relocation of a proton from the nitrogen atom to the oxygen atom in the primary amide group. 28 The proton transfer is often assisted by the nearby water molecule or gold surface. The catalytic effect of gold is also supported by the control experiments using chemically modified GNPs (Fig. S6). In the first half of the proton transfer process, one proton leaves the nitrogen atom to bind with the gold adatom of GNP, resulting in the deprotonated 4-MBAm structure in the junction as I1. The deprotonation of primary amide in plasmonic junctions at the neutral pH has been reported previously. This ionized intermediate needs to interact with the gold adatoms to be stabilized. The variety of binding configurations with the gold adatoms leads to a large variation in the spectra, as shown in the s-1 and s-2 signals. In the second half of the proton transfer process, the proton attached to the gold adatom binds with the oxygen atom to complete the tautomerization of amide. The resulted imidic acid form (I2) is often observed in the SERS measurements as s-3 signal. The signature v(C=N) peak of s-3 also reveals the presence of Au-N interaction for I2. The charge transfer from N to Au helps to stabilize the I2 structure.

The following two steps (3 and 4) of the reaction are the departure of the second proton from the nitrogen atom. Assisted by the hot electron, the second proton leaves the nitrogen atom to bind with the gold adatom of GNP, resulting in another deprotonated structure I3 corresponding to s-4 signal in the junction. It is worth noting that I3 has two structural isomers named as I3-1 and I3-2, in which the proton of O atom can flip from one position close to the N atom to another position away from the N atom. According to the calculation results, from I3-1 to I3-2, the C=N bond becomes slightly stronger, resulting in a higher wavenumber of the v(C=N) peak of I3-2 than that of I3-1. Only I3-2 can be transformed into T5 transition state. Based on the calculated v(C=N) peak of I3-2 near 1665 cm⁻¹, we found a few I3-2 signals in experiments (see Fig. S20). After losing two protons, the ionized nitrogen atom needs to interact strongly with the gold adatom to stabilize the charged I3. The relatively rare I3 signal in the experiment suggests the strong Au-N interaction is difficult to be established or short-lived.

Step 5 of the reaction is the deoxygenation, likely triggered by the movement of gold adatom interacting with the N atom of I3-2. When the gold adatom moves closer to the oxygen atom, the

gold adatom may interact with both the N and O atoms, promoting the formation of T5. Due to the Au-O interaction, the C-O bond is weakened while the C=N bond of I3-2 is strengthened towards a triple bond. The T5 is highly unstable, and the signature peak of $v(C \cong N)$ fluctuates greatly in the observed spectra (see Fig. 2d and S20 of SI). Finally, in step 6, with the further increased Au-O interaction, the C-O bond of T5 fully breaks and the product 4-MBN forms with the normal C $\equiv N$ bond (nitrile group), indicated by the stable signature peak near 2240 cm⁻¹ in the experiment. We also conducted intrinsic reaction coordinate (IRC) calculation along the reaction path from I3-2 to 4-MBN. The black line in Fig. 6c shows the single point energy change along the reaction path. The CN bond length (red line in Fig. 6c) of the structures along the forward pathway decreases continuously. The CN bond length dropped especially fast during the conversion from I3-2 to T5, revealing the significant change of the CN bond from the double bond to the triple bond.

The stretching of the CN bond contributes to the signature peak of most intermediates and product 4-MBN. The shortened CN bond length implies the blue-shift of the peak position of the v(CN). We have calculated the Raman spectra of several structures along the I3-2 to T5 reaction pathway (see Fig. 6c). In addition, we also calculated several structures of I2 with different C=N bond length induced by different Au-N interactions (see Fig. S18). Indeed, as shown in Fig. 6d, the peak position of v(CN) blue-shifted continuously from near 1500 cm⁻¹ of I2 to about 2000 cm⁻¹ of T5, which further extended to 2240 cm⁻¹ of 4-MBN. For comparison, we showed the representative SERS trajectories containing dynamic signals of I2, I3-2, and T5 in Fig. 6e. Three transient spectra are shown in Fig.6f for each intermediate. The significant fluctuations of the v(CN) peak in experiments match well with the CN bond length change induced v(CN) peak position changes in calculations.

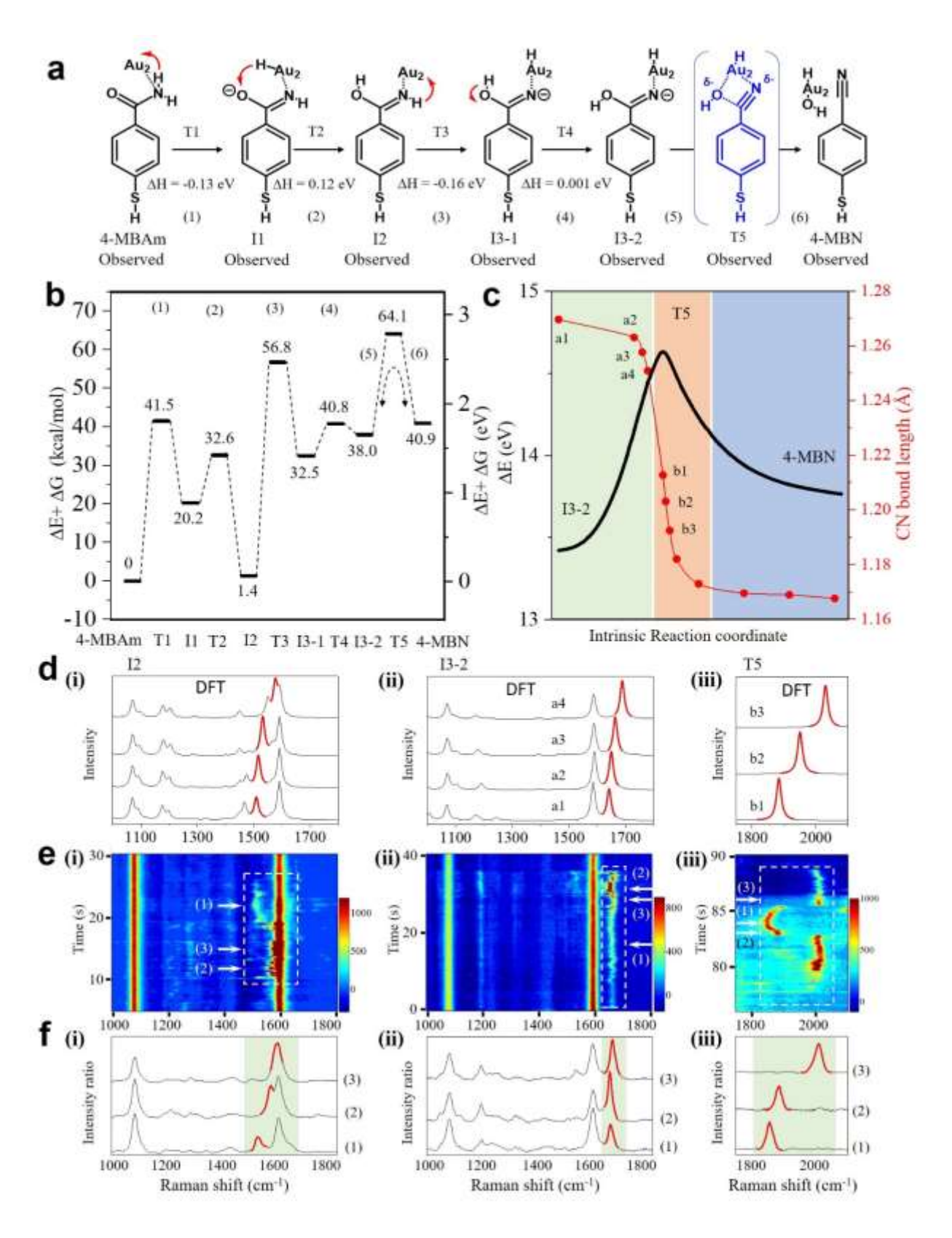


Figure 6 | The reaction path diagram and the energy calculations. **a.** The diagram of the proposed reaction path from 4-MBAm to 4-MBN in the plasmonic junctions. The structures of the transition states T1

to T4 are shown in Fig. S22. Δ H is the reaction enthalpy. **b.** The corresponding relative energies calculated by DFT for all the structures. **c.** The energy and CN bond length changes along the reaction path from I3-2 to 4-MBN. **d-f.** The calculated spectra (d), representative SERS trajectories (e), and the corresponding transient spectra (f) at the time pointed by the white arrows in (e) for I2 (i), I3-2 (ii) and T5 (iii). The signature peaks of v(CN) are shown in red color in (d) and (f). The structures corresponding to d(i) are discussed in Fig. S18.

It is also interesting to note that several intermediates can be observed with tens of seconds lifetime in the SERS measurements. The lifetime is surprisingly long, considering the much higher total energies of these intermediates. It has been reported that the nanoscale confinement of the nanocavities can reduce the entropy S.²⁹ Highly stable picocavity with lifetime longer than 1 s was also observed due to the metal-nitrile interactions in the plasmonc junctions.¹⁶ Here, the Au-N or Au-O interactions with the intermediates limit the freedom of the molecule thus reducing Δ S. Further, the local temperature is expected to be higher in the nano- or picocavity. Considering the Gibbs free energy Δ G= Δ H-T Δ S, where Δ H is the reaction enthalpy and T is the reaction temperature. The negative entropy change Δ S and higher local T in the junction will increase the Δ G of possible transformations for unstable intermediates. The higher Δ G thus reduces the transformation rate and stabilizes the intermediates for observation.

CONCLUSION

In summary, the plasmon-assisted hydration reaction from aromatic primary amide to aromatic nitrile has been successfully observed in real time by SERS in plasmonic molecular junctions formed in the NPoNE structures. In an aqueous solution with neutral pH at room temperature, the nitrile peak can be observed more than 80% of the time and about 40% of molecules in the hotspots are converted to 4-MBN irradiated by the low power laser, suggesting the reaction was effectively catalyzed by cooperative hot electron and GNP catalysis. In the time-resolved SERS measurements, stochastic and transient signals other than the signature peaks of 4-MBAm and 4-MBN are also observed in about 10% of the time. By using DFT calculations and the picocavity model, the origin of transient spectral changes can be explained reasonably well by gold adatom complexed reaction intermediates. We found that gold adatoms played crucial roles in the measurements. These dynamic and active gold adatoms may be generated due to the thermal fluctuations of surface gold atoms or the interactions with the immobilized molecules. They help to catalyze the reaction,

stabilize the otherwise short-lived intermediates, generate signature spectral changes, and provide enormous enhancement to the local optical field to boost the SERS signal. From the identified intermediates, we revealed the two proton transfer steps and the evolution of CN bond from single to double to triple during the dehydration reaction process. We also observed the reaction was reversible, providing insights for the metal catalyzed hydration reaction of nitrile to amide in water.³⁰ Further, we demonstrated that the molecule stabilized picocacvities on the gold surface are key to understand the stochastic and complicated SERS signals. The combined DFT (with picocavity model) and the *in situ* time-resolved SERS approach can be a valuable tool to gain mechanistic insight to complex multistep organic reactions catalyzed in plasmonic junctions.

EXPERIMENTAL METHODS

Chemicals. The 4-MBAm was synthesized as discussed in S1 of SI. Phosphate Buffered Saline (PBS) powder (pH 7.3-7.5) and Absolute Ethanol (200 proof) were purchased from Fisher Scientific. Potassium ferrocyanide (98.5%, analysis grade) was purchased from Acros Organics. Citrate stabilized 40 nm diameter GNPs were purchased from Ted Pella, Inc. All the aqueous solutions were prepared using deionized water (~18 M ohm) purified by the Purelab system of ELGA/Siemens.

SERS Measurements. SERS is performed on a home-built Raman microscopy setup based on a Nikon Ti-U microscope. Briefly, a 632.8 nm laser beam is focused by a 40x objective lens at the GNE apex that is placed in a liquid cell, which is installed on the microscope sample stage. The SERS trajectories are collected with a time resolution of 50 ms by a CCD camera (PIXIS 100B_eXcelon, Princeton Instrument). The spectral resolution is about 2 cm⁻¹. The typical laser power density on the GNE apex is 8.14 μW/μm².

The GNE (see S3 of SI) is used as the working electrode and the Ag/AgCl wire electrode is used as the quasi-reference electrode. All the measurements are performed at room temperature in electrolyte. The typical electrolyte is 10 mM PBS (pH 7.4). These GNEs gave no measurable SERS signals before GNP adsorptions, which is important to guarantee that the SERS signals are only from the molecules inside the hotspots of NPoNE structures. Initially, the liquid cell contains GNPs with a concentration of 150 pM. After stable 7a and 8a peaks are observed in the SERS

spectra (typically 12 mins), the GNP solution in the liquid cell is replaced with fresh 10 mM PBS solution. The GNP number density on the GNE apex is about 30/µm² based on the SEM images.

Data analysis. The SERS data were processed by custom programs written in Matlab and Labview, and OriginPro software. The background of the SERS spectra was removed after fitting by the Asymmetric-Least-Squares method (see Fig. S4). We also corrected the background effect³¹ for most individual spectra by background division. The intensity is changed to intensity ratio after background correction. To select the dynamic signals, we picked the signals with their intensity at last 5 times higher than the baseline noise and with both clear starting and ending points.

DFT calculations. DFT calculations were carried out with QuantumATK³² and Gaussian09³³ software packages. The energy calculation and the atomic structural optimization of the moleculegold cluster complexes were carried out with QuantumATK, which was based on the linear combination of atomic orbitals (LCAO) basis set approach. The calculation was carried out within the Generalized gradient approximation (GGA) with the Perdew-Burke-Ernzerhof (PBE) exchange-correlation functional.³⁴ The basis set was used at single zeta polarized level for Au atoms and double zeta polarized level for C, H, O, N and S atoms. To better simulate the electronic structure of gold nanostructures, we used the periodic gold crystal structures. In the next step, the Raman spectra of the optimized atomic geometries were calculated with Gaussian09 (see section 8 of SI). In Gaussian09, the PW91PW91 exchange-correlation functional³⁵ and 6-311g (d, p) basis set were used for molecules and the LANL2DZ effective core potential and basis set³⁶ were used for gold atoms. The calculated Raman spectra were plotted by applying a Lorentzian function with a full-width at half-height (FWHH) of 5 cm⁻¹. The scaling factor was set to 1.0056, which was close to the values previously used.³⁷ The calculations in Gaussian09 assumed a uniform EM field. To simulate the influence of the highly non-uniform electric field in picocavity, we followed the procedures reported by Shin, H. H et al.. 15 The details are given in S10 of SI.

AUTHOR INFORMATION

Corresponding Authors

*E-mail: feng liang@wust.edu.cn.

*E-mail: schang23@wust.edu.cn.

*E-mail: jinhe@fiu.edu.

ORCID:

Jianghao Zhou: 0000-0002-9317-9710

Jing Guo: 0000-0001-7292-6265

Alexander Moiseevich Mebel: 0000-0002-7233-3133

Govinda Ghimire: 0000-0003-2207-680X

Feng Liang: 0000-0002-3974-2621

Shuai Chang: 0000-0001-7405-5555

Jin He: 0000-0002-2633-9809

Notes

The authors declare no competing financial interest.

SUPPORTING INFORMATION

The Supporting Information is available free of charge at https://pubs.acs.org/doi/xxx.

Fabrication, surface modification and characterization of GNE, background correction, control experiments, detailed DFT calculation methods, the assignment of SERS peaks, extra data and reaction path calculations

ACKNOWLEDGEMENTS

This work is partially supported by NSF CHE-2003785. We acknowledge the computing resources provided by the Instructional & Research Computing Center (IRCC) at Florida International University.

REFERENCES

(1) Thompson, D. T. Using gold nanoparticles for catalysis. *Nano Today* **2007**, *2* (4), 40-43. DOI: 10.1016/s1748-0132(07)70116-0. Grirrane, A.; Corma, A.; García, H. Gold-Catalyzed Synthesis of Aromatic Azo Compounds from Anilines and Nitroaromatics. *Science* **2008**, *322* (5908), 1661-1664. DOI: 10.1126/science.1166401. Xie, W.; Walkenfort, B.; Schlucker, S. Label-free SERS monitoring of chemical reactions catalyzed by small gold nanoparticles using 3D plasmonic superstructures. *J Am Chem Soc* **2013**, *135* (5), 1657-1660. DOI: 10.1021/ja309074a.

(2) Frischkorn, C.; Wolf, M. Femtochemistry at Metal Surfaces: Nonadiabatic Reaction Dynamics. *Chemical Reviews* **2006**, *106* (10), 4207-4233. DOI: 10.1021/cr050161r. Manjavacas, A.; Liu, J. G.; Kulkarni, V.; Nordlander, P. Plasmon-Induced Hot Carriers in Metallic Nanoparticles. *ACS Nano* **2014**, *8* (8), 7630-7638. DOI: 10.1021/nn502445f. Zhou, L.; Swearer, D. F.; Zhang, C.; Robatjazi, H.; Zhao, H.; Henderson, L.; Dong, L.; Christopher, P.; Carter, E. A.; Nordlander, P.; Halas, N. J. Quantifying hot carrier and thermal contributions in plasmonic photocatalysis. *Science* **2018**, *362* (6410), 69-72. DOI: doi:10.1126/science.aat6967. Halas, N. J. Spiers Memorial Lecture. Introductory lecture: Hot-electron

- science and microscopic processes in plasmonics and catalysis. *Faraday Discuss* **2019**, *214*, 13-33. DOI: 10.1039/c9fd00001a.
- (3) Mukherjee, S.; Libisch, F.; Large, N.; Neumann, O.; Brown, L. V.; Cheng, J.; Lassiter, J. B.; Carter, E. A.; Nordlander, P.; Halas, N. J. Hot Electrons Do the Impossible: Plasmon-Induced Dissociation of H2 on Au. *Nano Lett.* **2013**, *13* (1), 240-247. DOI: 10.1021/nl303940z. Devasenathipathy, R.; Wang, J.-Z.; Xiao, Y.-H.; Rani, K. K.; Lin, J.-D.; Zhang, Y.-M.; Zhan, C.; Zhou, J.-Z.; Wu, D.-Y.; Tian, Z.-Q. Plasmonic Photoelectrochemical Coupling Reactions of para-Aminobenzoic Acid on Nanostructured Gold Electrodes. *J. Am. Chem. Soc.* **2022**, *144* (9), 3821-3832. DOI: 10.1021/jacs.1c10447.
- (4) Li, Z.; Kurouski, D. Plasmon-Driven Chemistry on Mono- and Bimetallic Nanostructures. *Accounts of Chemical Research* **2021**, *54* (10), 2477-2487. DOI: 10.1021/acs.accounts.1c00093.
- (5) Zrimsek, A. B.; Chiang, N.; Mattei, M.; Zaleski, S.; McAnally, M. O.; Chapman, C. T.; Henry, A.-I.; Schatz, G. C.; Van Duyne, R. P. Single-Molecule Chemistry with Surface- and Tip-Enhanced Raman Spectroscopy. *Chemical Reviews* **2017**, *117* (11), 7583-7613. DOI: 10.1021/acs.chemrev.6b00552. Choi, H.-K.; Lee, K. S.; Shin, H.-H.; Koo, J.-J.; Yeon, G. J.; Kim, Z. H. Single-Molecule Surface-Enhanced Raman Scattering as a Probe of Single-Molecule Surface Reactions: Promises and Current Challenges. *Accounts of Chemical Research* **2019**, *52* (11), 3008-3017. DOI: 10.1021/acs.accounts.9b00358.
- (6) Huh, H.; Trinh, H. D.; Lee, D.; Yoon, S. How Does a Plasmon-Induced Hot Charge Carrier Break a C–C Bond? *ACS Applied Materials & Interfaces* **2019**, *11* (27), 24715-24724. DOI: 10.1021/acsami.9b05509. (7) Zhao, Y.; Du, L.; Li, H.; Xie, W.; Chen, J. Is the Suzuki–Miyaura Cross-Coupling Reaction in the Presence of Pd Nanoparticles Heterogeneously or Homogeneously Catalyzed? An Interfacial Surface-Enhanced Raman Spectroscopy Study. *The Journal of Physical Chemistry Letters* **2019**, *10* (6), 1286-1291. DOI: 10.1021/acs.jpclett.9b00351.
- (8) Huang, Y.-F.; Zhu, H.-P.; Liu, G.-K.; Wu, D.-Y.; Ren, B.; Tian, Z.-Q. When the Signal Is Not from the Original Molecule To Be Detected: Chemical Transformation of para-Aminothiophenol on Ag during the SERS Measurement. *J. Am. Chem. Soc.* **2010**, *132* (27), 9244-9246. DOI: 10.1021/ja101107z.
- (9) Choi, H. K.; Park, W. H.; Park, C. G.; Shin, H. H.; Lee, K. S.; Kim, Z. H. Metal-Catalyzed Chemical Reaction of Single Molecules Directly Probed by Vibrational Spectroscopy. *J Am Chem Soc* **2016**, *138* (13), 4673-4684. DOI: 10.1021/jacs.6b01865.
- (10) Al-Huniti, M. H.; Croatt, M. P. Metal-Catalyzed Dehydration of Primary Amides to Nitriles. *Asian Journal of Organic Chemistry* **2019**, *8* (10), 1791-1799. DOI: 10.1002/ajoc.201900343.
- (11) Ganesan, M.; Nagaraaj, P. Recent developments in dehydration of primary amides to nitriles. *Organic Chemistry Frontiers* **2020**, *7* (22), 3792-3814, 10.1039/D0Q000843E. DOI: 10.1039/D0Q000843E.
- (12) Johansson, A.; Kollman, P.; Rothenberg, S.; McKelvey, J. Hydrogen bonding ability of the amide group. *J. Am. Chem. Soc.* **2002**, *96* (12), 3794-3800. DOI: 10.1021/ja00819a013. Krishnakumar, V.; Murugeswari, K.; Surumbarkuzhali, N. Molecular structure, intramolecular hydrogen bonding and vibrational spectral investigation of 2-fluoro benzamide--a DFT approach. *Spectrochim Acta A Mol Biomol Spectrosc* **2013**, *114*, 410-420. DOI: 10.1016/j.saa.2013.05.047.
- (13) Chen, Z.; Chen, W.; Zhang, L.; Fu, W.; Cai, G.; Zheng, A.; Tang, T. Acidic hierarchical porous ZSM-5 assembled palladium catalyst: A green substitute to transform primary amides to nitriles. *Applied Catalysis B: Environmental* **2022**, *302*, 120835. DOI: https://doi.org/10.1016/j.apcatb.2021.120835. (14) Benz, F.; Schmidt, M. K.; Dreismann, A.; Chikkaraddy, R.; Zhang, Y.; Demetriadou, A.; Carnegie, C.; Ohadi, H.; De, N. B.; Esteban, R. Single-molecule optomechanics in "picocavities". *Science* **2016**, *354* (6313), 726-729.
- (15) Shin, H. H.; Yeon, G. J.; Choi, H. K.; Park, S. M.; Lee, K. S.; Kim, Z. H. Frequency-Domain Proof of the Existence of Atomic-Scale SERS Hot-Spots. *Nano Lett* **2018**, *18* (1), 262-271. DOI: 10.1021/acs.nanolett.7b04052.

- (16) Carnegie, C.; Griffiths, J.; de Nijs, B.; Readman, C.; Chikkaraddy, R.; Deacon, W. M.; Zhang, Y.; Szabo, I.; Rosta, E.; Aizpurua, J.; Baumberg, J. J. Room-Temperature Optical Picocavities below 1 nm(3) Accessing Single-Atom Geometries. *J Phys Chem Lett* **2018**, *9* (24), 7146-7151. DOI: 10.1021/acs.jpclett.8b03466.
- (17) Guo, J.; Pan, J.; Chang, S.; Wang, X.; Kong, N.; Yang, W.; He, J. Monitoring the Dynamic Process of Formation of Plasmonic Molecular Junctions during Single Nanoparticle Collisions. *Small* **2018**, *14* (15), e1704164. DOI: 10.1002/smll.201704164.
- (18) Castro, J. L.; Lopez-Ramirez, M. R.; Arenas, J. F.; Soto, J.; Otero, J. C. Evidence of deprotonation of aromatic acids and amides adsorbed on silver colloids by surface-enhanced Raman scattering. *Langmuir* **2012**, *28* (24), 8926-8932. DOI: 10.1021/la204702w.
- (19) Huang, M.; Zhou, Q.; Liang, F.; Yu, L.; Xiao, B.; Li, Y.; Zhang, M.; Chen, Y.; He, J.; Xiao, S.; Chang, S. Detecting Individual Bond Switching within Amides in a Tunneling Junction. *Nano Lett.* **2021**, *21* (12), 5409-5414. DOI: 10.1021/acs.nanolett.1c01882.
- (20) Kwasnieski, D. T.; Wang, H.; Schultz, Z. D. Alkyl-Nitrile Adlayers as Probes of Plasmonically Induced Electric Fields. *Chem Sci* **2015**, *6* (8), 4484-4494. DOI: 10.1039/C5SC01265A. Westley, C.; Fisk, H.; Xu, Y.; Hollywood, K. A.; Carnell, A. J.; Micklefield, J.; Turner, N. J.; Goodacre, R. Real-Time Monitoring of Enzyme-Catalysed Reactions using Deep UV Resonance Raman Spectroscopy. *Chemistry* **2017**, *23* (29), 6983-6987. DOI: 10.1002/chem.201701388.
- (21) Hanif, S.; Liu, H.; Chen, M.; Muhammad, P.; Zhou, Y.; Cao, J.; Ahmed, S. A.; Xu, J.; Xia, X.; Chen, H.; Wang, K. Organic Cyanide Decorated SERS Active Nanopipettes for Quantitative Detection of Hemeproteins and Fe(3+) in Single Cells. *Anal Chem* **2017**, *89* (4), 2522-2530. DOI: 10.1021/acs.analchem.6b04689.
- (22) Tobisu, M.; Xu, T.; Shimasaki, T.; Chatani, N. Nickel-catalyzed Suzuki-Miyaura reaction of aryl fluorides. *J Am Chem Soc* **2011**, *133* (48), 19505-19511. DOI: 10.1021/ja207759e. Aggarwal, R. L.; Farrar, L. W.; Saikin, S. K.; Andrade, X.; Aspuru-Guzik, A.; Polla, D. L. Measurement of the absolute Raman cross section of the optical phonons in type Ia natural diamond. *Solid State Communications* **2012**, *152* (3), 204-209. DOI: 10.1016/j.ssc.2011.11.005. Juergensen, S.; Kusch, P.; Reich, S. Resonant Raman Scattering of 4-Nitrothiophenol. *physica status solidi* (b) **2020**, *257* (12), 2000295. DOI: 10.1002/pssb.202000295.
- (23) García-Álvarez, R.; Crochet, P.; Cadierno, V. Metal-catalyzed amide bond forming reactions in an environmentally friendly aqueous medium: nitrile hydrations and beyond. *Green Chem.* **2013**, *15* (1), 46-66. DOI: 10.1039/c2gc36534k.
- (24) Zhang, R.; Zhang, Y.; Dong, Z. C.; Jiang, S.; Zhang, C.; Chen, L. G.; Zhang, L.; Liao, Y.; Aizpurua, J.; Luo, Y.; Yang, J. L.; Hou, J. G. Chemical mapping of a single molecule by plasmon-enhanced Raman scattering. *Nature* **2013**, *498* (7452), 82-86. DOI: 10.1038/nature12151. Martin Sabanes, N.; Ohto, T.; Andrienko, D.; Nagata, Y.; Domke, K. F. Electrochemical TERS Elucidates Potential-Induced Molecular Reorientation of Adenine/Au(111). *Angew Chem Int Ed Engl* **2017**, *56* (33), 9796-9801. DOI: 10.1002/anie.201704460.
- (25) Mojica, E.-R. E.; Abbas, N.; Wyan, L. O.; Vedad, J.; Desamero, R. Z. B. Solvent Sensitivity of the −C≡ N Group: A Raman Spectroscopic Study. In *Raman Spectroscopy in the Undergraduate Curriculum*, ACS Symposium Series, Vol. 1305; American Chemical Society, 2018; pp 181-197.
- (26) Kim, K.; Lee, J. W.; Shin, K. S. Cyanide SERS as a platform for detection of volatile organic compounds and hazardous transition metal ions. *Analyst* **2013**, *138* (10), 2988-2994, 10.1039/C3AN00105A. DOI: 10.1039/C3AN00105A.
- (27) Asakawa, H.; Lee, K. H.; Lin, Z.; Yamashita, M. Facile scission of isonitrile carbon-nitrogen triple bond using a diborane(4) reagent. *Nat Commun* **2014**, *5*, 4245. DOI: 10.1038/ncomms5245. Mencos, A.; Krim, L. Isomerization and fragmentation of acetonitrile upon interaction with N(4S) atoms: the chemistry of nitrogen in dense molecular clouds. *Monthly Notices of the Royal Astronomical Society* **2016**, *460* (2), 1990-1998. DOI: 10.1093/mnras/stw1102 (acccessed 5/24/2022).

- (28) Nagashima, K.; Takatsuka, K. Electron-wavepacket reaction dynamics in proton transfer of formamide. *J Phys Chem A* **2009**, *113* (52), 15240-15249. DOI: 10.1021/jp905583s. Al-Zaqri, N.; Khatib, T.; Alsalme, A.; Alharthi, F. A.; Zarrouk, A.; Warad, I. Synthesis and amide imidic prototropic tautomerization in thiophene-2-carbohydrazide: XRD, DFT/HSA-computation, DNA-docking, TG and isoconversional kinetics via FWO and KAS models. *RSC Advances* **2020**, *10* (4), 2037-2048, 10.1039/C9RA09831C. DOI: 10.1039/C9RA09831C.
- (29) Riss, A.; Paz, A. P.; Wickenburg, S.; Tsai, H. Z.; De Oteyza, D. G.; Bradley, A. J.; Ugeda, M. M.; Gorman, P.; Jung, H. S.; Crommie, M. F.; Rubio, A.; Fischer, F. R. Imaging single-molecule reaction intermediates stabilized by surface dissipation and entropy. *Nat Chem* **2016**, *8* (7), 678-683. DOI: 10.1038/nchem.2506.
- (30) Shimizu, K.-i.; Kubo, T.; Satsuma, A.; Kamachi, T.; Yoshizawa, K. Surface Oxygen Atom as a Cooperative Ligand in Pd Nanoparticle Catalysis for Selective Hydration of Nitriles to Amides in Water: Experimental and Theoretical Studies. *ACS Catalysis* **2012**, *2* (12), 2467-2474. DOI: 10.1021/cs3006154.
- (31) Lin, K. Q.; Yi, J.; Zhong, J. H.; Hu, S.; Liu, B. J.; Liu, J. Y.; Zong, C.; Lei, Z. C.; Wang, X.; Aizpurua, J.; Esteban, R.; Ren, B. Plasmonic photoluminescence for recovering native chemical information from surface-enhanced Raman scattering. *Nat Commun* **2017**, *8* (1), 14891. DOI: 10.1038/ncomms14891.
- (32) Smidstrup, S.; Markussen, T.; Vancraeyveld, P.; Wellendorff, J.; Schneider, J.; Gunst, T.; Verstichel, B.; Stradi, D.; Khomyakov, P. A.; Vej-Hansen, U. G.; Lee, M. E.; Chill, S. T.; Rasmussen, F.; Penazzi, G.; Corsetti, F.; Ojanpera, A.; Jensen, K.; Palsgaard, M. L. N.; Martinez, U.; Blom, A.; Brandbyge, M.; Stokbro, K. QuantumATK: an integrated platform of electronic and atomic-scale modelling tools. *J Phys Condens Matter* **2020**, *32* (1), 015901. DOI: 10.1088/1361-648X/ab4007.
- (33) Frisch, M.; Trucks, G. S., H.; ; Scuseria, G.; Robb, M.; Cheeseman, J.; Scalmani, G.; Barone, V.; Mennucci, B.; Petersson, G. A.; al., e. *Gaussian 09, Revision D. 01*; Gaussian, Inc., 2009.
- (34) Perdew, J. P.; Burke, K.; Ernzerhof, M. Generalized gradient approximation made simple. *Physical review letters* **1996**, *77* (18), 3865. Perdew, J. P.; Burke, K.; Ernzerhof, M. Generalized Gradient Approximation Made Simple[Phys. Rev. Lett. 77, 3865 (1996)]. *Physical Review Letters* **1997**, *78* (7), 1396-1396. DOI: 10.1103/PhysRevLett.78.1396.

(35) Perdew, J. P. In Electronic Structure of Solids, Ziesche, P., Eschrig, a. H. Eds.; Akademie Verlag, 1991;

- p 11. Perdew, J. P.; Chevary, J. A.; Vosko, S. H.; Jackson, K. A.; Pederson, M. R.; Singh, D. J.; Fiolhais, C. Atoms, molecules, solids, and surfaces: Applications of the generalized gradient approximation for exchange and correlation. *Phys Rev B Condens Matter* **1992**, *46* (11), 6671-6687. DOI: 10.1103/physrevb.46.6671. Perdew, J. P.; Burke, K.; Wang, Y. Generalized gradient approximation for the exchange-correlation hole of a many-electron system. *Phys Rev B Condens Matter* **1996**, *54* (23), 16533-16539. DOI: 10.1103/physrevb.54.16533. Adamo, C.; Barone, V. Exchange functionals with improved long-range behavior and adiabatic connection methods without adjustable parameters: The mPW and mPW1PW models. *The Journal of Chemical Physics* **1998**, *108* (2), 664-675. DOI: 10.1063/1.475428. K. Burke; J. P. Perdew; Wang, a. Y. Derivation of a Generalized Gradient Approximation: The PW91 Density Functional. In *Electronic Density Functional Theory: Recent Progress and New Directions*, J. F. Dobson, G. Vignale, Das, a. M. P. Eds.; Springer, Boston, MA, 1998; p 81. (36) Hay, P. J.; Wadt, W. R. Ab initio effective core potentials for molecular calculations. Potentials for the transition metal atoms Sc to Hg. *The Journal of Chemical Physics* **1985**, *82* (1), 270-283. DOI:
- (37) Lewandowski, H.; Koglin, E.; Meier, R. J. Computational study of the infrared spectrum of acetic acid, its cyclic dimer, and its methyl ester. *Vibrational Spectroscopy* **2005**, *39* (1), 15-22. DOI: 10.1016/j.vibspec.2004.10.003. Sun, M.; Fang, Y.; Zhang, Z.; Xu, H. Activated vibrational modes and

299-310. DOI: 10.1063/1.448975.

10.1063/1.448799. Hay, P. J.; Wadt, W. R. Ab initio effective core potentials for molecular calculations. Potentials for K to Au including the outermost core orbitals. *The Journal of Chemical Physics* **1985**, *82* (1),

Fermi resonance in tip-enhanced Raman spectroscopy. *Phys Rev E Stat Nonlin Soft Matter Phys* **2013**, *87* (2), 020401. DOI: 10.1103/PhysRevE.87.020401.

TOC

